Supplemental Information

3D Printable Biopolymers as Pelvic Floor Scaffolds

Lindsay B. Chambers,[a&] Yuxiang Zhu,[b&] Churan Yu,[a] Natalie Crutchfield,[e] Jixin Hou,[a] Liang Liang,[c] Xianqiao Wang,[d] Yang Liu,[e] M. Taylor Sobczak,[a] Taylor Theobald,[a] Xiao Sun,[f] Carly R. Stoll,[g] Tiffany V. Pulido,[g] Johnny Yi,[h] Jeffrey L. Cornella,[i] Heather McIlwee,[j] Hitesh Handa,[e] Elizabeth J. Brisbois,[e] Jessica N. Lancaster,[g] and Kenan Song[k]*

[a] *Department of Mechanical Engineering, School of Environmental, Civil, Agricultural and Mechanical (ECAM), College of Engineering, University of Georgia, Athens, GA, 30602*

[b] *School of Manufacturing Systems and Networks, Ira A. Fulton Schools of Engineering, Arizona State University, Mesa, AZ, USA 85212*

[c] *123Techs Inc., Athens, GA, 30602*

[d] *School of Environmental, Civil, Agricultural Mechanical (ECAM), College of Engineering, University of Georgia, Athens, GA, 30602*

[e] *Department of Biomedical Engineering, School of Chemical, Materials, and Biomedical Engineering (CMBE), College of Engineering, University of Georgia, Athens, GA, 30602*

[f] *Department of Mechanical and Industrial Engineering, College of Engineering, Northeastern University, Boston, MA, 02115*

[g] *Department of Immunology, Mayo Clinic Arizona, 13400 E Shea Blvd, Scottsdale, AZ, 85259 USA*

[h] *Department of Obstetrics and Gynecology, Mayo Clinic Arizona, 13400 E Shea Blvd, Scottsdale, AZ, 85259 USA*

[i] *Department of Medical and Surgical Gynecology, Mayo Clinic Arizona, 5777 E Mayo Blvd, Phoenix, AZ, 85054 USA*

[j] *School of Environmental, Civil, Agricultural Mechanical (ECAM), College of Engineering, University of Georgia, Athens, GA, 30602; Regenerative Bioscience Center, UGA, Athens, GA, 30602*

[&] *Co-first author*

[*] *Corresponding author Email: kenan.song@uga.edu*

Table of Contents

1. Current State of the Art of Polymer Tissue Scaffolds

Table S1. Summary of mechanical and bio-functions of current polymer tissue scaffolds:

Manufacturing conditions			Mechanical properties			Bio-functions		Ref.
Materials	**Processing**	**Microstructures**	**E' (MPa)**	**σ (MPa)**	**ε (%)**	**biocompatibility**	**biodegradability**	
PVA, Cellulose	FT and ECH crosslinking	Porous	1.4-2.8 $*10^{-3}$	N/A	N/A	N/A	Yes	[1]
PVA, Cellulose	ECH crosslinking only	Porous	(62-409) $*10^{-6}$	N/A	N/A	N/A	Yes	
PVA, Silk fibroin	Boric acid crosslinking	Porous	N/A	0.04-0.18	N/A	Yes	Yes	[2]
PLA	Electrospinning	Randomly scattered fibers	4.5 ± 2.9	0.72 ± 0.18 MPa	N/A	Yes	Yes	[3]
PVA, CS, CNT, strong acids	Electrospinning, gaseous crosslinking	Randomly scattered fibers	130	N/A	N/A	Yes	No	[4]
PVA, Collagen, GA	Electrospinning, GA crosslinking	Randomly scattered fibers	1	N/A	55-65 %	Yes	Yes	[5]
Chitosan	microwave-assisted crosslinking	Randomly porous	N/A	1	N/A	Yes	No	[6]
PET	Knitting/weaving	Porous	0.0276	N/A	N/A	Yes	No	[7]
PLA and ciprofloxacin hydrochloride (CIP)	Electrospinning	Randomly scattered fibers	N/A	N/A	N/A	Yes	No	[8]
PVA	3D printing and crosslinking	Tunable pores and porosity	4.88	2.12	100	Yes	Yes	This work

Abbreviations: CNT=carbon nanotube; CS=chitosan; ECH=epichlorohydrin; FT=freeze/thaw; GA=glutaraldehyde, PET= polyethylene terephthalate

Table S1 provides a summary of various materials and their respective mechanical properties, biocompatibility, and biodegradability in the context of pelvic organ prolapse (POP) tissue scaffolds. Different crosslinking strategies and microstructures have been employed to enhance scaffold properties. For instance, PVA combined with cellulose or silk fibroin and crosslinked via methods like freeze-thaw (FT) and epichlorohydrin (ECH) results in porous structures with varied biodegradability and biocompatibility. Electrospinning methods produce randomly scattered fiber structures with polymers like PLA, PVA, and collagen, where crosslinking agents such as glutaraldehyde (GA) improve mechanical properties and biocompatibility, making them more favorable for POP applications. Notably, the PVA scaffold developed in this work exhibits tunable porosity, high tensile strength (4.88 MPa), and high elongation at break (100%), while also demonstrating both biocompatibility and biodegradability, highlighting its potential as a superior alternative for POP treatment compared to other materials listed in the table. This tunable structure, achieved through 3D printing and crosslinking, allows for precise control over scaffold mechanical and bio-functional properties, potentially improving patient outcomes in POP repair.

2. Spectral Studies of the POP Scaffolds:

FTIR analysis was performed with a UATR loading method on a Spectrum 3 spectrometer (Perkin Elmer, Greenville, SC), capturing absorbance readings across the infrared spectra from 4000–650 cm−1. In the FTIR results, the broad peak at 3300 cm^{-1} confirms the presence of alcohol groups in both the neat and crosslinked samples, while the distinct peak at 1050 cm^{-1} in the crosslinked sample indicates C-O stretching, attributed to the alcohol groups within the DTT moiety. The green region in the figure represents the C-O stretch between 1260-1050 cm^{-1}. All methods and materials are detailed in the manuscript and this Supplementary Information.

The FTIR spectra is included in the SI. To address this question, the FTIR spectra in the supplementary information provide evidence of successful photopolymerization during the UV curing process. In the spectra, the neat PVA (upper plot) shows typical PVA peaks, while the PVA prototype (lower plot) exhibits additional peaks that are indicative of crosslinking. The broad peak around 3330 cm^{-1} corresponds to the hydroxyl (OH) groups, while the sharp peak near 1050 cm^{-1}, present in the PVA prototype, suggests C–O stretching from crosslinked functional groups. The presence of these peaks in the prototype spectrum confirms the thiol-ene crosslinking reaction, which is initiated by UV light during 3D printing. This crosslinking provides the structural integrity required for the scaffold to maintain its shape and stability in physiological conditions. The FTIR data thus supports the conclusion that UV-induced photopolymerization effectively contributes to the scaffold's initial crosslinked network.

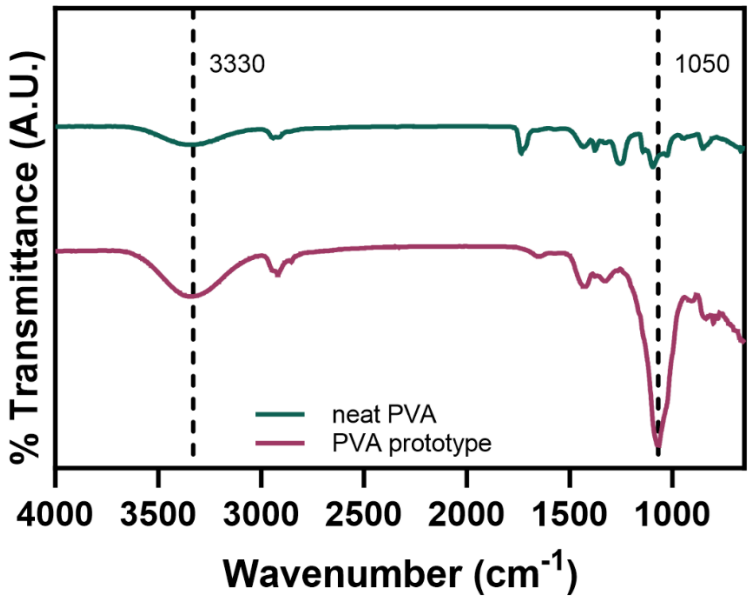

Figure S1. FTIR spectra of unfunctionalized PVA and our prototype. The distinct O-H stretch at 3330 cm^{-1} and the C-O stretch at 1050 cm^{-1} are marked with dotted lines.

3. Submersed Fatigue Test Method:

Samples were analyzed using a TA Instruments RSA-G2 Dynamic Mechanical Analyzer (DMA) for fatigue testing, utilizing an immersion system throughout all tests. Prior to testing, samples were immersed in tap water (pH = 7) for 2 hours, with tap water also used to fill the immersion system during testing. The temperature was maintained at 37°C (i.e., human body temperature), and a harmonic strain was applied at a frequency of 1 Hz. Strain levels were incrementally increased from 10% to 15%, 20%, and 24%, with each level sustained for 1,000 cycles. The loading gap was set to 5 mm for all samples, and each sample was tested once for demonstration purposes.

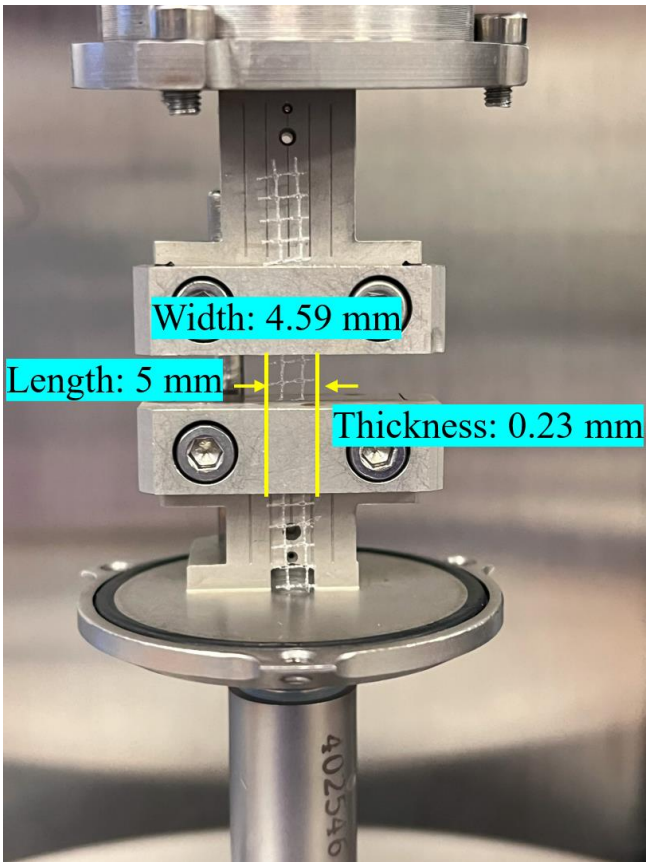

Figure S2. Restorelle in the immersion fatigue testing geometry before the immersion was applied. Note that the width measurement for DMA, UTS, and fatigue were collected consistently via this method.

This immersion fatigue test graph illustrates the evolution of the storage modulus (E') for PVA and several commercially available meshes (Progrip, Ventralight, 3DMax, Restorelle, Vertessa) under cyclic strain conditions (10% to 24%) over 4000 cycles. The PVA scaffold shows a consistent and relatively stable modulus across different strain levels, maintaining its structural integrity over the test duration, which highlights its resilience under repetitive mechanical loading in wet conditions. In contrast, most commercial meshes show significant fluctuations, with Progrip and 3DMax exhibiting sharp decreases in modulus at higher strain percentages or more fatigue cycles. This trend indicates that PVA's mechanical properties may be more reliable under fatigue conditions, making it a promising candidate for dynamic environments such as pelvic organ support.

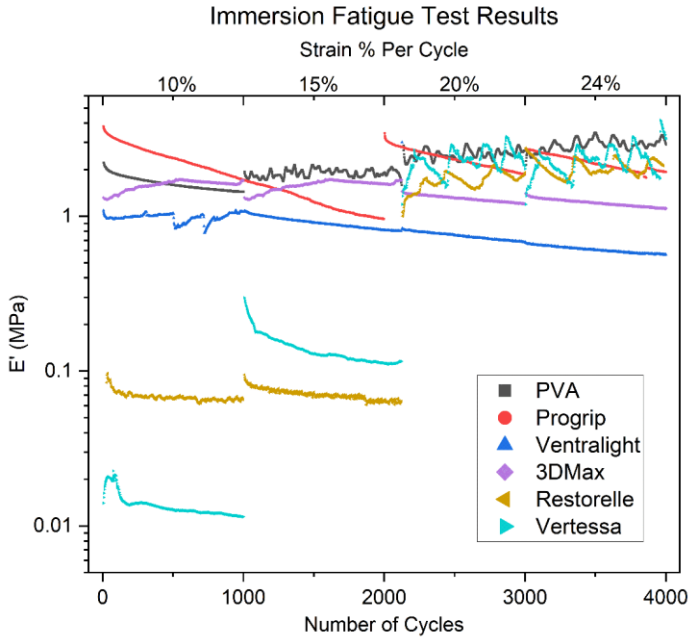

Figure S3. Fatigue tests of hernia and pelvic organ support mesh. Biodesign was not included as it consists primarily of ECM material.

4. Biological Methods:

Mice: C57BL/6J mice were maintained under specific pathogen-free conditions in the Mayo Clinic animal facility and sourced from Jackson Laboratories. For all experiments, 6-8 week-old female mice were used. Mouse maintenance and experimental procedures were carried out with approval from the Institutional Animal Care and Use Committee at the Mayo Clinic.

Surgical Procedure: PVA scaffolds were cut to 0.5-cm^2 pieces and corners were rounded to minimize irritation. Scaffolds were soaked in sterile 70% ethanol for 2 hours, rinsed in sterile saline, and dried in a sterile hood before sterilization by UV light for 15 minutes each side. Mice were pre- and post-operatively treated with Carprofen and Ethiqa for pain management. Mice were anesthetized using isoflurane prior to surgical preparation and access of the abdominal area. Implants were placed in the right intraperitoneal space away from the surgical site, and the surgical access site resutured. In sham surgeries, no scaffolds were placed. The peritoneum was closed using simple interrupted suturing with 5-0 vicryl suture (Ethicon, J493G). Weight was monitored over four weeks at indicated timepoints to monitor health and surgical site was inspected daily for two weeks for signs of discomfort and infection. At the conclusion of the experiment, mice were humanely euthanized, and skin was peeled away from the abdominal wall in order to lavage the intraperitoneal cavity with saline. For scaffold extraction, the abdominal space was accessed, careful to avoid the area of the scaffold, and the tissue around the scaffold was cut away. Scaffolds were immersed in 10% formalin for 24 hours.

Flow Cytometric Analysis: Up to 10^5 cells were incubated for 20 minutes on ice in 100 μL of fetal bovine serum-supplemented saline buffer with fluorochrome-conjugated antibodies directed against the following mouse targets: CD11b-FITC (M1/70, BD Bioscience, 553310), CD11c-BV711 (N418, BioLegend, 117349), F4/80-PerCp (BM8, BioLegend, 123126), Ly6C-APC-Cy7 (HK1.4, BioLegend, 128025), Ly6G-BV510 (1A8, BioLegend, 127633), CD3-BUV395 (17A2, BD Biosciences, 740268), B220-BV605 (RA3-6B2, BioLegend, 103243), MHCII-PE-Cy7 (M5, BioLegend, 107630). Antibodies were diluted 1:200 from stock concentrations of 0.5 mg ml^{-1} Cells were washed and resuspended in 10 μg ml^{-1} propidium iodide (PI) to determine viability. Samples were analyzed on a Symphony flow cytometer (BD Biosciences) and data were analyzed using FlowJo (v.10, TreeStar). Cell count was determined using FlowJo and graphed in GraphPad Prism (v10.1.0). Statistical analysis was performed in GraphPad Prism.

Histological Evaluation: The preserved implanted meshes and surrounding tissues were submitted for paraffin embedding and slide preparation by the Histopathology Core Laboratory at the Mayo Clinic. Slides were stained with Hematoxylin and Eosin (H&E) and Masson's trichrome (MT) stain. Images were captured using an Olympus BX45 microscope using cellSens (v2.3) imaging software.

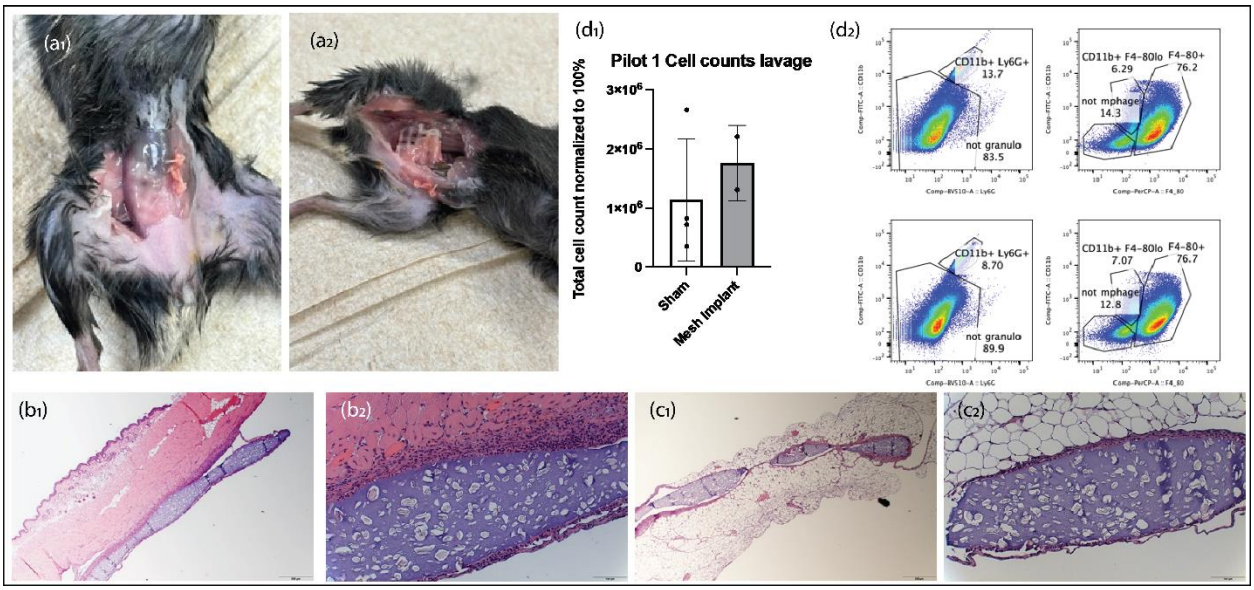

Figure S4. (a1) Healthy skin outside the scaffold does not show indications of inflammation. (a2) Scaffold exposed to indicate placement in mice. (b1) muscle attachment to scaffold, (b2) closer look at muscle attachment to scaffold. (c1) Fat pad attachment to scaffold, (c2) closer look at fat pad attachment to scaffold. (d1) Flow cytometry data and (d2) histology data. Scale bars 100 µm for (b1) and (c1), 50 µm for (b2) and (c2).

5. **References:**

(1) Chang, C.; Lue, A.; Zhang, L. Effects of Crosslinking Methods on Structure and Properties of Cellulose/PVA Hydrogels. *Macromol. Chem. Phys.* **2008**, *209* (12), 1266–1273. https://doi.org/10.1002/macp.200800161.

(2) Lee, J.; Sultan, Md.; Kim, S.; Kumar, V.; Yeon, Y.; Lee, O.; Park, C. Artificial Auricular Cartilage Using Silk Fibroin and Polyvinyl Alcohol Hydrogel. *Int. J. Mol. Sci.* **2017**, *18* (8), 1707. https://doi.org/10.3390/ijms18081707.

(3) Mangera, A.; Bullock, A. J.; Roman, S.; Chapple, C. R.; MacNeil, S. Comparison of Candidate Scaffolds for Tissue Engineering for Stress Urinary Incontinence and Pelvic Organ Prolapse Repair. *BJU Int.* **2013**, *112* (5), 674–685. https://doi.org/10.1111/bju.12186.

(4) Mombini, S.; Mohammadnejad, J.; Bakhshandeh, B.; Narmani, A.; Nourmohammadi, J.; Vahdat, S.; Zirak, S. Chitosan-PVA-CNT Nanofibers as Electrically Conductive Scaffolds for Cardiovascular Tissue Engineering. *Int. J. Biol. Macromol.* **2019**, *140*, 278–287. https://doi.org/10.1016/j.ijbiomac.2019.08.046.

(5) Jahanbani, Y.; Davaran, S.; Yousefi, M.; Roshangar, L.; Bastani, P.; Kadkhoda, J. Fabrication and Characterization of COL/PVA Nanofiber Scaffolds for Soft Tissue Engineering. *Chem. Methodol.* **2024**, *8* (5). https://doi.org/10.48309/chemm.2024.455838.1794.

(6) Radwan-Pragłowska, J.; Stangel-Wójcikiewicz, K.; Piątkowski, M.; Janus, Ł.; Matýsek, D.; Majka, M.; Amrom, D. The Potential of Novel Chitosan-Based Scaffolds in Pelvic Organ Prolapse (POP) Treatment through Tissue Engineering. *Molecules* **2020**, *25* (18), 4280. https://doi.org/10.3390/molecules25184280.

(7) Maurer, M.; Röhrnbauer, B.; Feola, A.; Deprest, J.; Mazza, E. Prosthetic Meshes for Repair of Hernia and Pelvic Organ Prolapse: Comparison of Biomechanical Properties. *Materials* **2015**, *8* (5), 2794–2808. https://doi.org/10.3390/ma8052794.

(8) Liu, M.; Wang, L.; Tong, X.; Dai, J.; Li, G.; Zhang, P.; Li, H. Antibacterial Polymer Nanofiber-Coated and High Elastin Protein-Expressing BMSCs Incorporated Polypropylene Mesh for Accelerating Healing of Female Pelvic Floor Dysfunction. *Nanotechnol. Rev.* **2020**, *9* (1), 670–682. https://doi.org/10.1515/ntrev-2020-0052.